Ultrasonics 93 (2019) 71–80

Contents lists available at ScienceDirect

Ultrasonics

journal homepage: www.elsevier.com/locate/ultras

Characterizing excitability of Lamb waves generated by electromagnetic acoustic transducers with coupled frequency domain models

Shen Wang[a,*], Songling Huang[a], Qing Wang[b], Zhe Wang[a], Wei Zhao[a]

[a] State Key Lab. of Power System, Dept. of Electrical Engineering, Tsinghua University, Beijing 100084, China
[b] Department of Engineering, Durham University, DH1 3LE Durham, United Kingdom

ARTICLE INFO

Keywords:
Electromagnetic acoustic transducers (EMATs)
Excitability of Lamb waves
Coupled frequency domain model

ABSTRACT

Electromagnetic acoustic transducers (EMATs) are versatile non-contact ultrasonic transducers with relatively low transduction efficiency. A fundamental problem not answered completely yet is how the structure of an EMAT influences the generation of various Lamb wave modes. We tackle this problem with fully coupled frequency domain EMAT models where the underlying integro-differential equations are solved directly and the magnitudes of the phasors of the displacement components at a point in the middle plane of a plate are used to represent the strength of the S0 and A0 mode waves. Idealized single-wire, two-wire and wire bundle EMATs with uniform bias magnetic field and practical meander line and tightly wound EMATs with distributed bias field are studied. Polar plots of the idealized EMATs with swept angle of the bias field show that the vertical component of the bias field decides the strength of the S0 mode waves. Sweeping of the width of the magnet for the practical EMATs generates S0 mode curves that could be explained from the distribution of the vertical component of the bias field. This work represents the first attempt to solve the proposed problem of characterizing excitability of Lamb waves with EMATs quantitatively, via the model-based approach.

1. Introduction

Traditionally piezoelectric transducers are used to generate ultrasonic waves in elastic solids in ultrasonic testing. Generally liquid coupling is required to transmit the generated waves into the solid sample under investigation. Liquid coupling is not convenient sometimes and uncertainty might be introduced because of this coupling. As complements to piezoelectric transducers, non-contact transducers such as air-coupled transducers and electromagnetic acoustic transducers (EMATs) are more and more attractive in industry. In this work we focus on the EMATs.

EMATs are normally composed of the permanent magnet, the current-carrying coil and the tested metal sample, i.e. the sample is one component of the transducer because it is involved in the transduction process. In non-magnetic material testing, the ultrasonic waves are driven by the Lorentz forces excited by the interaction between the eddy currents induced in the metal sample by the current-carrying coil and the bias magnetic field. In magnetic material testing, magnetostriction also takes effect, rendering the working mechanism even more complex. Coupling is not required for the EMATs, and a small air gap can exist between the coil and the sample, so the EMATs could be used in some special situations like testing hot or moving samples. EMATs are versatile, in that they could be used to generate various types of ultrasonic bulk and guided waves with different configurations of the bias magnet and the coil [1–4].

Despite these obvious advantages of EMATs, they also have limitations including low transduction efficiency, being only applicable on conductive and ferromagnetic materials, requirement for specialized instrumentation, etc. [5–7]. The low efficiency means a reliable model of the transducer is crucial for theoretical study and industrial applications. However, building a model of an EMAT is not an easy task. This is because the EMAT model is multi-physics in nature, requiring knowledge from both the electromagnetic field and the elastodynamic field, and how to couple them is not straightforward. Here we summarize some of the important work in this field. Ludwig and Dai conducted transient analysis of a meander coil EMAT placed on isotropic non-ferromagnetic half-space, assuming uniform static magnetic field [8]. Kaltenbacher et al. reported modeling of meander coil EMAT for transmitting and receiving plate waves, and optimization of magnet width to reduce the amplitude of undesired A0 mode waves [9,10]. Jafari-Shapoorabadi et al. studied in detail the controlling eddy current equations and argued that the total current divided by the cross section area of the conductor was used as the source current density in the previous work, and this meant the incomplete equation was applied and

* Corresponding author.
E-mail address: wangshen@mail.tsinghua.edu.cn (S. Wang).

https://doi.org/10.1016/j.ultras.2018.10.013
Received 31 January 2018; Received in revised form 22 September 2018; Accepted 29 October 2018
Available online 31 October 2018
0041-624X/

the skin effect and the proximity effect were ignored [11], while we proved that these effects were not ignored even with the incomplete equations in [12] via solving the underlying differential equations directly with the COMSOL FEM package. The code in [11] was later incorporated in [4] for the optimization of an EMAT with a racetrack coil. Dhayalan and Balasubramaniam built the electromagnetic model of a meander EMAT in COMSOL, and the simulated Lorentz force was exported to another package Abaqus as the driving force to excite Lamb waves [13]. The above-mentioned modeling work only involves non-magnetic materials. There is also some initial work on modeling EMATs used to test magnetic material, while we will not discuss further here.

A fundamental and important problem while using EMATs for the generation of Lamb waves is how the structures of the transduers influence the excitation of the different Lamb wave modes. Nagy et al. studied the relationship between the direction of the traction force and the generation of the S0 and A0 modes, and the distribution of the bias magnetic field [14], shedding some light on this issue, but the force vector was spatially uniformly distributed and the bias field was not connected with the Lamb waves, indicating that the electromagnetic and elastodynamic effects were in fact modeled separately and the model was not truly coupled. Nevertheless, it was revealed that the distributions of the bias magnetic field and the eddy current, and hence the Lorentz force, influence the generated wave modes greatly.

It is not difficult to tell that a model-based solution to the proposed problem requires that,

1. The model should be multiphysical and the related physics should be coupled, so that the model is correct and accurate theoretically.
2. It should be easy to compute the model so that detailed study of the problem is feasible.
3. A method must be developed to clearly differentiate various Lamb wave modes that might be excited simultaneously.

In this work we try to answer these requirements in characterizing the excitability of Lamb waves generated by the EMATs quantitatively through a modeling approach. We implement in COMSOL the complete coupled models of the EMATs, in which the electromagnetic and elastodynamic effects happen at the same time. A mid level approach is adopted to solve the underlying integro-differential equations directly so the physics is fully controlled. The models are in the frequency domain so that the computation is fast. The Lamb wave modes are differentiated by evaluating different displacement components at the middle plane of the plate, an idea from [15,16].

Specifically, the formulations of the Lorentz-force EMATs are introduced first. Then modeling of the EMATs is discussed. One group of idealized EMATs including the single-wire EMAT, the two-wire EMAT and the wire bundle EMAT, and another group of practical EMATs including the meander line EMAT and the tightly wound EMAT are considered. Finally the process to characterize the excitability of Lamb waves with these EMATs is described.

2. Formulations of the Lorentz-force EMATs

In this section we summarise the basic equations in the multiphysics models of the Lorentz force EMATs used to generate Lamb waves in an aluminum plate. The equations come from the electromagnetic and elastodynamic fields.

2.1. The electromagnetic equations

The basic equations for the electromagnetic field simulation in the study of the EMATs are Maxwell's equations [17],

$$\nabla \times \mathbf{E} = -\frac{\partial \mathbf{B}}{\partial t} \tag{1}$$

$$\nabla \times \mathbf{H} = \mathbf{J}_f + \frac{\partial \mathbf{D}}{\partial t} \tag{2}$$

$$\nabla \cdot \mathbf{D} = \rho_f \tag{3}$$

$$\nabla \cdot \mathbf{B} = 0 \tag{4}$$

These equations are Faraday's law, Ampère-Maxwell law, Gauss's law for electric fields and Gauss's law for magnetic fields, respectively. $\mathbf{E}$ is the electric field, $\mathbf{B}$ is the magnetic flux density, t is the time variable, $\mathbf{H}$ is the magnetic field strength, $\mathbf{J}_f$ is the free current density, $\mathbf{D}$ is the electric flux density, ρ_f is the free charge density. $\nabla\times$ is curl of a vector, and $\nabla\cdot$ is divergence of a vector. Since the frequency in the normal operation of an EMAT is no higher than several MHz, the term $\frac{\partial \mathbf{D}}{\partial t}$ (the displacement current density) in Maxwell's equations could be neglected.

To solve Maxwell's equations, another set of equations called the constitutive equations are needed,

$$\mathbf{B} = \mu \mathbf{H} \tag{5}$$

$$\mathbf{D} = \epsilon \mathbf{E} \tag{6}$$

in which μ is the magnetic permeability, and ϵ is the dielectric constant. μ and ϵ are scalars here, indicating that the material is linear.

When modeling the magnetic field of the permanent magnet in a magnetostatic simulation, we start from the relation of $\mathbf{B}$ and $\mathbf{H}$ in matter,

$$\begin{aligned}\mathbf{B} &= \mu_0(\mathbf{H} + \mathbf{M}) = \mu_0(\mathbf{H} + \chi_m \mathbf{H} + \mathbf{M}_0) \\ &= \mu \mathbf{H} + \mu_0 \mathbf{M}_0 = \mu \mathbf{H} + \mathbf{B}_r\end{aligned} \tag{7}$$

in which $\mathbf{M} = \chi_m \mathbf{H} + \mathbf{M}_0$ is the magnetization vector, $\mathbf{M}_0$ is the remanent magnetization, and $\mathbf{B}_r = \mu_0 \mathbf{M}_0$ is the remanent flux density. In region without free currents, (2) is reduced to $\nabla \times \mathbf{H} = 0$ and this leads to the definition of magnetic scalar potential V_m as $\mathbf{H} = -\nabla V_m$. Combining this with (4), we arrive at

$$\nabla \cdot (-\mu \nabla V_m + \mathbf{B}_r) = 0 \tag{8}$$

This equation is solved with the magnetostatic sub-model.

With the magnetic vector potential (MVP) $\mathbf{A}$, the equation describing the eddy current phenomenon is,

$$-\frac{1}{\mu}\nabla^2 \mathbf{A} + \sigma \frac{\partial \mathbf{A}}{\partial t} = \mathbf{J}_s \tag{9}$$

in which ∇^2 is the vector Laplacian operator and $\mathbf{J}_s$ is the source current density. The eddy current density, not written explicitly in (9), is $\mathbf{J}_e = -\sigma \frac{\partial \mathbf{A}}{\partial t}$. This equation holds where there exists a conductor and a source current flows in the conductor.

For 2D planar field simplification where $\mathbf{J}_s$ is assumed to be along the z axis, we have $\mathbf{J}_s = J_{sz}\mathbf{e}_z$, with J_{sz} as the z component of vector $\mathbf{J}_s$, and $\mathbf{e}_z$ as the unit vector along the z axis. Similarly we also have $\mathbf{A} = A_z \mathbf{e}_z$. If we write A_z as A and J_{sz} as J_s, the vector equation (9) is transformed to the z component scalar equation,

$$-\frac{1}{\mu}\nabla^2 A + \sigma \frac{\partial A}{\partial t} = J_s \tag{10}$$

This equation is a diffusion equation describing the eddy current phenomenon. Now the eddy current density is $J_e = -\sigma \frac{\partial A}{\partial t}$.

The externally applied total current i is the surface integral of the total current density J_t, which is the sum of the source current density J_s and the eddy current density J_e,

$$i = \iint_S J_t \, dS = \iint_S (J_s + J_e) \, dS \tag{11}$$

in which S is the cross section of the source conductor. In a 2D planar model where the conductor is assumed to be long and straight, J_s is uniformly distributed, then together with (10), we have,

$$-\frac{1}{\mu}\nabla^2 A + \sigma\frac{\partial A}{\partial t} = \frac{i + \iint_S \sigma\frac{\partial A}{\partial t}\, dS}{S} \tag{12}$$

This is the equation designated as *complete* in the study of EMATs [18].

For steady state or frequency-domain analysis, the phasor notation is adopted,

$$-\frac{1}{\mu}\nabla^2 \dot{A} + \mathrm{j}\omega\sigma\dot{A} = \frac{\dot{i} + \mathrm{j}\omega\sigma \iint_S \dot{A}\, dS}{S} \tag{13}$$

The dots on A and i indicate they are complex phasors. ω is the angular frequency. j is the imaginary unit. This frequency-domain integro-differential equation was proposed by Konrad [19]. It should be noted that (12) and (13) hold for source conductors. In non-source conductors like the metal plate the J_s term in (10) is dropped, while in non-conducting region the eddy current term J_e is also dropped.

Eqs. (12) and (13) are exactly what we solve in this work with the mid-level approach as described in [12]. In this way, the underlying physics is fully controlled.

2.2. The elastodynamic equations

The equations describing the generation and propagation of the ultrasonic waves in an elastic solid are [20],

$$\nabla\cdot\mathbf{T} = \rho\frac{\partial^2\mathbf{u}}{\partial t^2} - \mathbf{F} \tag{14}$$

$$\mathbf{T} = \mathbf{c}:\mathbf{S} \tag{15}$$

$$\mathbf{S} = \nabla_s\mathbf{u} \tag{16}$$

These equations are equation of motion, Hooke's law and strain-displacement relation respectively. $\mathbf{T}$ is the stress tensor, $\nabla\cdot\mathbf{T}$ is its divergence, ρ is the density, $\mathbf{F}$ is the body force density, $\mathbf{c}$ is the stiffness tensor, $\mathbf{S}$ is the strain tensor, and $\mathbf{u}$ is the displacement vector. : is the double dot product of a fourth rank tensor $\mathbf{c}$ and a second rank tensor $\mathbf{S}$. $\nabla_s\mathbf{u}$ is the symmetric part of the gradient of the vector $\mathbf{u}$. It should be noted that the same symbol ρ was also used to represent the charge density in Maxwell's equations, and this shouldn't cause misunderstanding in this paper.

For homogenous and isotropic media, we have Navier's equation [21],

$$\mu\nabla^2\mathbf{u} + (\lambda+\mu)\nabla(\nabla\cdot\mathbf{u}) = \rho\frac{\partial^2\mathbf{u}}{\partial t^2} - \mathbf{F} \tag{17}$$

Here λ and μ are Lamé constants. Like the symbol ρ, the symbol μ was also used to represent the magnetic permeability. For 2D plane strain problems like modeling Lamb waves propagating in a plate, we have components of displacement vector $\mathbf{u}$ as $u_x = u = u(x, y, t)$, $u_y = v = v(x, y, t)$ and $u_z = w = 0$.

2.3. Lorentz force - link between the electromagnetic field and the elastodynamic field

The link between the electromagnetic field and the elastodynamic field is the volume Lorentz force density defined as,

$$\mathbf{F}_L = \mathbf{J}\times\mathbf{B} = \mathbf{J}\times(\mathbf{B}_0 + \mathbf{B}_d) \tag{18}$$

in which $\mathbf{B}$ is the total magnetic flux density composed of the static flux density $\mathbf{B}_0$ of the bias magnet, and the dynamic flux density $\mathbf{B}_d$ generated by the excitation coil. Usually for excitation current with moderate magnitude, the $\mathbf{B}_d$ term is very small compared with $\mathbf{B}_0$. We will use relatively small excitation currents in this work and thus neglect the $\mathbf{B}_d$ term.

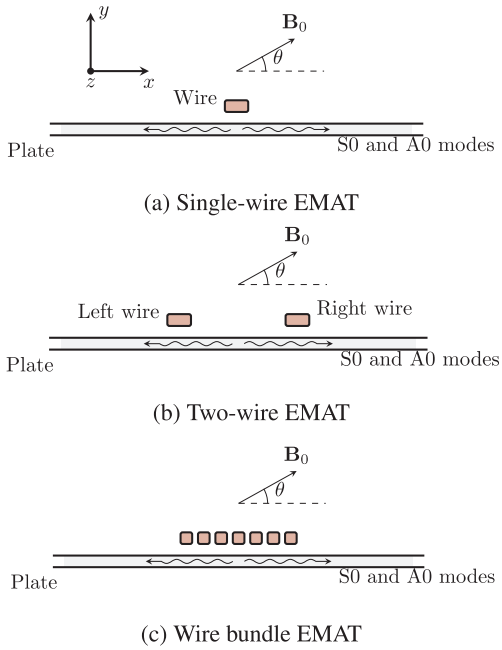

Fig. 1. Idealized EMATs with uniformly distributed bias magnetic field.

3. Modeling of the Lorentz-force EMATs

3.1. The modeling process

In this work we differentiate two groups of EMATs. The first group contains 'idealized' EMATs including the single-wire EMAT (Fig. 1a), the two-wire EMAT (Fig. 1b) and the wire bundle EMAT (Fig. 1c) with uniformly distributed bias magnetic field. We call them 'idealized EMATs' because the bias field is actually always distributed and cannot be uniform, and the single-wire coil and the two-wire coil are too simple. Although these EMATs are idealized, they could provide insights into the working mechanism of more complex EMATs. The single-wire EMAT could be thought of as a building block of more complex EMATs. The horizontal distance of the wires in the two-wire EMAT is exactly one-half wavelength of the S0 mode Lamb waves. When the electric currents in the two wires are in opposite directions, the S0 mode waves generated by the wires should add constructively, and this two-wire EMAT could be regarded as a building block of the popular meander line EMAT which will be discussed later. On the contrary, if the currents are in the same direction, the S0 mode waves should be suppressed. For the wire bundle EMAT, the multiple wires with electric currents in the same direction are closely placed to simulate a tightly wound coil. This corresponds to an alternative design of EMATs, with examples such as the EMAT with a spiral/pancake coil [22] and the EMAT with a racetrack coil.

Before details of these models are given, it is helpful to define some symbols as in Table 1. For the idealized EMATs, it is unnecessary to compute the magnetic field of the magnet, so the model contains one eddy current sub-model simulating the distribution of the eddy currents and the accompanying skin and proximity effects, and an

Table 1
Definitions of some symbols.

W_W	Width of the wire
H_W	Height of the wire
W_C	Width of the coil
W_M	Width of the magnet
H_M	Height of the magnet
l_M	Liftoff of the magnet
l_C	Liftoff of the coil (and wire)

elastodynamic sub-model simulating the generation and propagation of Lamb waves. The eddy current sub-model is composed of the surrounding air, the coil, and the middle section of the aluminum plate. The geometry of the elastodynamic sub-model consists of only the full plate. This design is valid because the eddy currents and the resulted Lorentz forces are concentrated in the local region of the plate just under the coil, so in the eddy current sub-model, only the middle section of the plate needs to be considered. The Lorentz forces are transfered to the elastodynamic sub-model as the driving forces of Lamb waves. By dividing the whole model into two geometries and two sub-models, we obtain some benefits. One advantage is that the structure of the whole model is very clear, in contrast to some of the previous work where different geometries and physics were mingled together. Another advantage is that we can apply different meshing rules to the same object (the aluminum plate) in different geometries according to respective underlying physics, thus reducing the total number of the elements.

The wires and the plate are assumed to be infinitely long in the z direction so a 2D model is valid. The plate section in the geometry of the eddy current sub-model is 300 mm in width and 1 mm in height. The wires have rectangular cross sections. $W_W = 2$ mm for the single-wire and two-wire EMATs, and $W_W = 1$ mm for the wire bundle EMAT. For all the wires $H_W = 1$ mm. The total currents in the wires are all $i = 1$ A. For the two-wire EMAT we will investigate the case of opposite currents and the case of currents in the same direction.

For the two-wire EMAT, the horizontal distance between the centers of the wires is half of the wavelength λ_{S0} of the S0 mode Lamb waves (Note that λ was also used to represent one of the Lamé constants), calculated from the phase velocity C_P and the frequency f. The frequency is chosen to be 250 kHz. With this frequency and a plate thickness of 1 mm, only the S0 and A0 modes exist, and the phase velocity of the S0 mode as determined from the phase velocity dispersion curves is $C_P = 5389.25$ m/s, then the wavelength is $\lambda_{S0} = C_P/f = 21.557$ mm. We developed a Matlab program to produce the phase velocity dispersion curves shown in Fig. 2, with Young's modulus $E = 70\times10^9$ Pa, Poisson's ratio $\nu = 0.33$, and the mass density $\rho = 2700$ kg/m^3. The liftoff value is $l_C = 0.5$ mm. The conductivity of the aluminum plate is 3.774×10^7 S/m, and the conductivity of the copper wires is 5.998×10^7 S/m. The magnetic permeabilities of these two materials are the same as that of the air, i.e. $\mu_0 = 1.2566\times10^{-6}$ H/m. A layer of infinite elements is added to the boundary of the air region to increase the modeling accuracy in the eddy current analysis. Fillets are added to the sharp corners of the wires, so that the singularities are removed, at the expense of an increased number of elements.

For the single-wire EMAT, the two-wire EMAT with opposite currents in the wires and the wire bundle EMAT, the total current density J_t

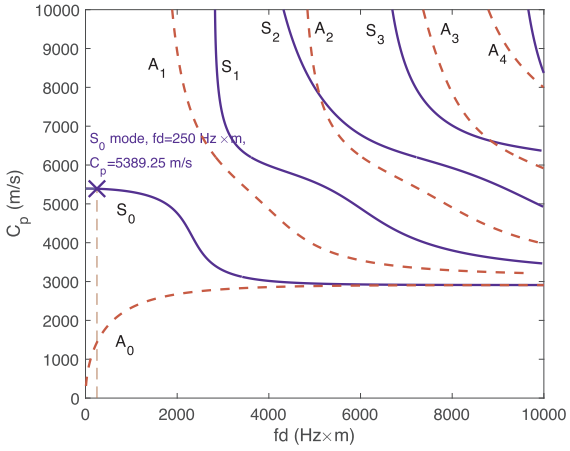

Fig. 2. Phase velocity dispersion curves of an aluminum plate. The operating point is marked with ×.

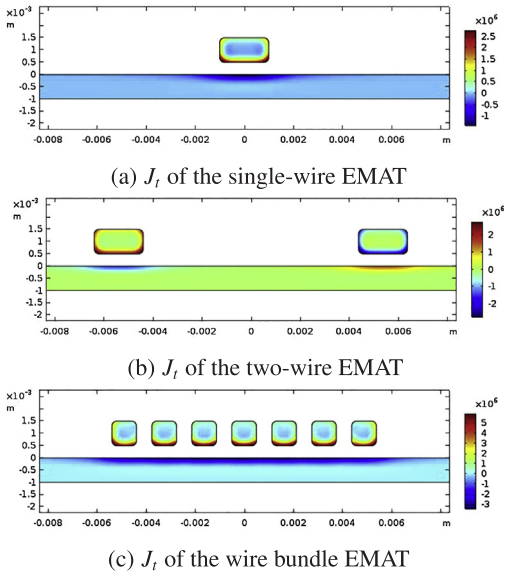

Fig. 3. Total current density (J_t) in the source conductors and the plates, for the idealized EMATs.

in the coil and the plate is simulated and drawn in Fig. 3 to validate the frequency domain solutions of the eddy current sub-models. It is easy to test that the integral of the total current density in every wire is 1 A ($\iint_S J_t\, dS = 1$ (A) where S is the cross section of the wire). The total current density concentrates at the surfaces of the source conductors and the plates, as predicted by the skin effect. In Fig. 3c the distribution of the total current density at the leftmost and rightmost wires is different from that at the middle wires, which clearly shows the proximity effect. It could also be observed in Fig. 3c that the eddy currents in the plate excited by the wires are joined together so that they work as a whole.

The geometry of the elastodynamic sub-model only consists of the full aluminum plate with a total length of 1.2 m. Lamé constants are $\lambda = 5.1\times10^{10}$ Pa and $\mu = 2.6\times10^{10}$ Pa, consistent with Young's modulus and Poisson's ratio given previously. In the transient analysis serving as a reference, the ends of the plate are free, and the total time of simulation is limited to avoid end reflection in the recorded waveforms of the displacement components. In the frequency domain model, perfectly matched layers (PMLs) are added to the ends of the plate to allow the wave energy to dissipate, which proves to be a crucial step of modeling. Two observation points (left and right) to record the displacement components are 0.2 m from the center of the transducer and in the middle plane of the plate. We are mainly concerned with the right point.

The other group of EMATs are 'practical' EMATs, because the distributions of the magnetic fields of the magnets are now considered. In this group we consider the meander line EMAT (Fig. 4a) and the tightly wound EMAT (Fig. 4b). The meander line coil structure represents a popular configuration of EMATs where the distance of adjacent wires is one-half wavelength and the currents in two adjacent wires are in opposite directions. The tightly wound EMAT is similar to the wire bundle EMAT in the group of idealized EMATs, and the only difference is that now a magnet is included in the model.

For these practical EMATs, another magnetostatic sub-model simulating the bias magnetic field is added to the model, and the two electromagnetic sub-models share the same geometry. For the magnet $W_M = 0.1$ m (this variable will be swept in Section 4), $H_M = 0.12$ m and $l_M = 0.002$ m. The material of the magnet is air, in accordance with example models shipped with COMSOL. The remanent flux density is 1 T along the y direction. The total currents in the wires are all $i = 1$ A (magnitude). For the meander line EMAT, there are 7 parallel wires,

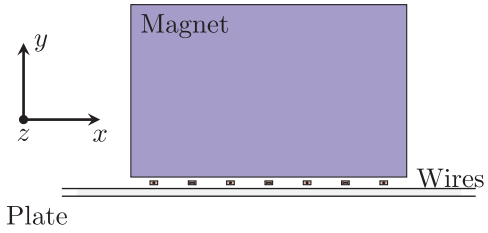

(a) Meander line EMAT

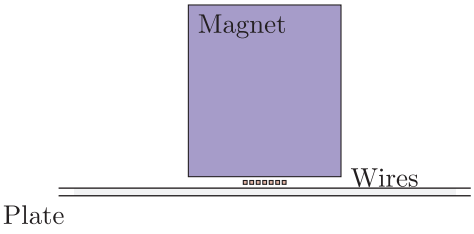

(b) Tightly wound EMAT

Fig. 4. Practical EMATs with distributed bias magnetic fields.

and the currents in two adjacent wires are in opposite directions. The horizontal distance between the centers of two adjacent wires is half of the wavelength as in the two-wire EMAT. The dimensions of the wires are $W_W = 2\,\text{mm}$ and $H_W = 1\,\text{mm}$. For the tightly wound EMAT, $W_W = 1\,\text{mm}$. Fillets are also added to the sharp corners of the magnets of these EMATs. Other settings of the models of the practical EMATs are the same as those of the idealized EMATs and will not be repeated here.

An explanation about the modeling of the physical phenomena is still missing. As stated in Section 2.1, the electromagnetic sub-models are solved using a mid-level approach where the underlying electromagnetic equations are specified precisely, so that they are under full control. Readers might refer to [12] for further information. We believe this is beneficial for exploratory studies of EMAT modeling where static and time-varying fields both exist and non-standard multi-physics coupling is involved.

3.2. Time-domain models vs. frequency domain models

Because we want to evaluate how the structure of an EMAT influences the generated Lamb waves, we must find a method to clearly differentiate the Lamb wave modes and quantify their strength. In [16], the authors proposed to solve the displacement components at the middle plane of the plate, then from the displacement wave structures of Lamb waves in a steel plate of 10 mm thickness at 50 kHz, the in-plane component (u) corresponds to the S0 mode only while the out-of-plane component (v) corresponds to the A0 mode only. From our dispersion curves calculation program which also has the ability to solve the wave structures at the selected operating point, this is also true for Lamb waves in an aluminum plate with a thickness of 1 mm at 250 kHz. So in the FEM models, we record the displacement component u at the observation points in the middle plane of the plate as the S0 mode Lamb waves, and the displacement component v as the A0 mode Lamb waves. The amplitudes of u and v will be used to represent the strength of the S0 and A0 modes. While the question remains of how to compute the u and v displacement components. We will compare three approaches[1] to compute u, with the meander line EMAT as an example. v could be calculated in the same way.

The first approach is implemented with the time-domain models, in which the bias magnetic field (for the practical EMATs) comes from the magnetostatic simulation while the eddy current distribution, and the generation and propagation of the Lamb waves are from time-dependent simulations. A time-stepping scheme is used for this simulation. For convergence of the time-dependent solver in COMSOL, a very small time step must be used, which means the simulation will be time-consuming. In this work, the number of time steps is set to 8000. The tone-burst excitation signal $x(t)$ is composed of 5 sinusoidal periods and modulated with a Hanning window function. Once the time waveform $u(t)$ at the observation point is simulated, the amplitude/peak of the envelope of this waveform will be solved as,

$$p_u = \mathscr{P}(|u(t) + \mathrm{j}\mathscr{H}[u(t)]|) \tag{19}$$

in which j is the imaginary unit, $\mathscr{H}[\cdot]$ is the Hilbert transform, $f + \mathrm{j}\mathscr{H}[f]$ is the analytic signal corresponding to the time domain signal f, and the absolute value of this analytic signal gives the envelope. $\mathscr{P}$ means solving the peak of the envelope. If there's only one wave packet in the time waveform, the maximum value of the envelope corresponds to its peak.

The second approach is to transform the input time-continuous excitation signal to its frequency components via the Fourier transform (implemented with the FFT on a computer), feed them into a frequency domain model, transform the output back into the time-response with inverse Fourier transform (implemented with the IFFT), and finally solve the peak of the envelope of the time waveform of displacement component u. Not all the frequency components are used, and a threshold value is set to select only the bigger frequency components.

The time waveform of u obtained in this way can be expressed as,

$$u(t) = \mathscr{F}^{-1}\{\mathscr{F}[x(t)]H_u(\omega)\} \tag{20}$$

in which $\mathscr{F}$ represents the Fourier transform, $\mathscr{F}^{-1}$ is the inverse Fourier transform, $x(t)$ is the input tone burst signal, $H_u(\omega)$ is the system function for the displacement component u. As the next step, the amplitude/peak is solved just like in Eq. (19). This approach will be less time-consuming than the time-domain simulation, since only tens of (or fewer) frequency components are enough, as selected by the threshold value. For this approach, we build a coupled frequency-domain model of the meander line EMAT, in which the bias magnetic field is again from the magnetostatic simulation, but the eddy current sub-model and the elastodynamic sub-model are completely in the frequency-domain. Then we implement this proposed approach by connecting the frequency-domain model in COMSOL with the Matlab environment where the FFT/IFFT processing is realized. The time waveform from this approach is carefully compared with the waveform from the previous time domain simulation, which serves as a reference. As an example, u waveforms from the time-dependent simulation and the frequency domain model with FFT/IFFT processing are compared in Fig. 5. The parameters of the EMAT are $W_M = 0.1\,\text{m}$, $H_M = 0.12\,\text{m}$, $l_M = 0.002\,\text{m}$ and $l_C = 0.0005\,\text{m}$. The threshold to select the frequency components is 1%, that is, only the frequency components higher than 1% of the peak value of the spectrum are used, and the others are discarded. With this threshold, 29 components around the center frequency of 250 kHz are kept.

One important requisite to validate the frequency domain model is that the whole model must be linear. In other words, the frequency model can't handle the part of the Lorentz force resulted from the dynamic magnetic field, because two complex phasors cannot be multiplied together to produce another phasor.

Since we are mostly concerned with the amplitude of the u waveform, yet another approach exists, where only one frequency is used in the frequency model, corresponding to a traditional steady state analysis. That is, we only consider the center frequency of the burst signal (250 kHz), and use the absolute value of the complex phasor to approximate the amplitude of the waveform. This process could be formulated as,

$$|\dot{u}| = |H_u(\omega_c)| \tag{21}$$

[1] These approaches were already discussed extensively in [23], where optimization of an omni-directional EMAT was conducted.

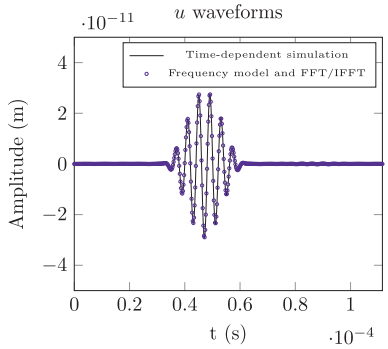

Fig. 5. u waveforms from time-dependent simulation and frequency domain model with FFT/IFFT processing.

in which ω_c is the center frequency in radian, $\dot{u}$ is the complex phasor of u.

It's still necessary to prove that the third approach is an acceptable approximation of the second approach. By carefully observing Eq. (21), we can see that $|\dot{u}|$ is the system function evaluated at the center frequency. While in Eq. (20), the spectrum of the tone burst signal $\mathscr{F}[x(t)]$ is bell-shaped, i.e. narrow-banded, and concentrated around the center frequency, so the result of $\mathscr{F}^{-1}[\cdot]$ operation is mainly decided by the value of the system function $H_u(\omega)$ at the center frequency ω_c, no matter what the system function looks like at other frequencies. Then a higher value of $H_u(\omega_c)$ means higher amplitude of the time waveform, and thus higher peak value of its envelope. So the absolute value of the phasor could be used to approximate the amplitude of the waveform. Corresponding to Fig. 5, the u system function is shown in Fig. 6.

The amplitudes of u from the second approach (frequency domain model with FFT/IFFT) and the third approach (single frequency model) are solved numerically with fixed $H_M = 0.12\,\text{m}$, $l_M = 0.002\,\text{m}$, $l_C = 0.0005\,\text{m}$ and different W_M values, to further validate the third approach. The results are shown in Fig. 7. p_u is the peak value of the envelope of u waveform solved with the frequency domain model and FFT/IFFT, while $|\dot{u}|$ is the magnitude of u phasor solved with one single frequency in the frequency domain model. These displacements are recorded at a point (the right point) 0.2 m away from the transducer and at the middle plane of the plate, as explained before. It could be observed that although the amplitudes from these two approaches are not identical, they have the same shapes.

The third approach is the fastest, since only one frequency is used. In the next section, we will mainly use this approach.

4. Characterizing the EMATs with the frequency domain models

In this section we characterize excitability of Lamb waves with the two groups of EMATs using the frequency domain models (with one single frequency). The quantities to evaluate are $|\dot{u}|$ and $|\dot{v}|$ representing

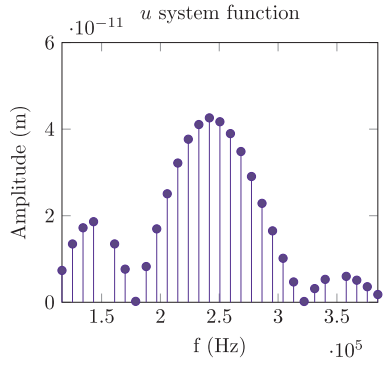

Fig. 6. u system function.

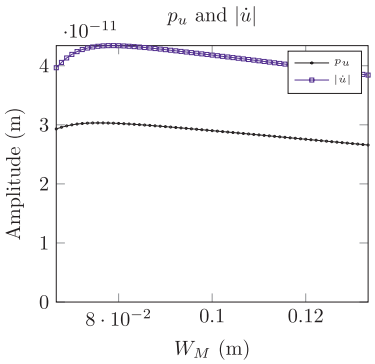

Fig. 7. u amplitudes at different W_M values, from the second and third approaches. $H_M = 0.12\,\text{m}$, $l_M = 0.002\,\text{m}$ and $l_C = 0.0005\,\text{m}$ are fixed.

the amplitudes of the S0 and A0 modes respectively. We will mainly analyze the influence of the bias magnetic field.

4.1. The single wire EMAT

Firstly, it would be interesting to investigate the behavior of the single-wire EMAT in Fig. 1a. The parameters of this EMAT were already introduced. Horizontally the wire is placed at the center of the model, and the phasors $\dot{u}$ and $\dot{v}$ of the displacement components u and v at two points (left and right) 0.2 m away from the center of the model and at the middle plane of the plate are calculated with different angle θ of the bias magnetic flux density with fixed magnitude of $B_0 = 1\,\text{T}$. This sweeping of the θ parameter is accomplished with a simple parametric study in COMSOL. For this configuration, the bias magnetic field is uniform for a fixed value of θ, while the eddy currents in the source wire and the plate are distributed.

In Fig. 8 is the result of sweeping the θ parameter at the right point in the middle plane of the plate. The absolute values of the $\dot{u}$ and $\dot{v}$ phasors are drawn with respect to θ in the polar plot. From the figure, we can observe that the magnitude of $|\dot{u}|$ increases from around zero to some maximum value with θ increasing from 0° to 90°. When θ increases from 90° to 180°, $|\dot{u}|$ decreases to around zero. The other half of the curve is symmetric with respect to the line representing $\theta = 0°$ and $\theta = 180°$. The curve of $|\dot{v}|$ has similar shape but is rotated counterclockwise (or clockwise) 90°, with a slight tilt. Another notable characteristic of the $|\dot{v}|$ curve is that although $|\dot{v}|$ reaches its minimum with $\theta = 90°$ but this minimum is not near zero with respect to its maximum value. We can conclude from the plot that a vertical force ($\theta = 0°$) in the skin depth region of the plate excites almost no S0 mode waves and maximum A0 mode waves, and a horizontal force ($\theta = 90°$) excites maximum S0 mode waves together with some A0 mode waves.

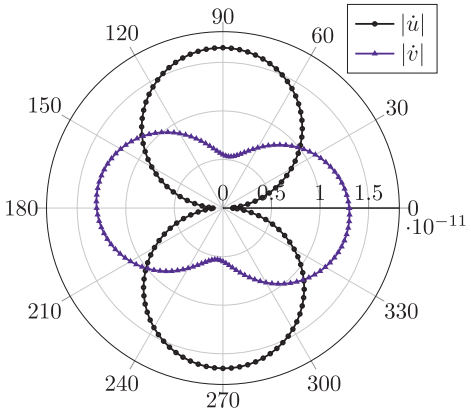

Fig. 8. Variations of the amplitudes of the S0 and A0 modes ($|\dot{u}|$ and $|\dot{v}|$) with the angle of the bias field (θ) at the right point, for the single-wire EMAT.

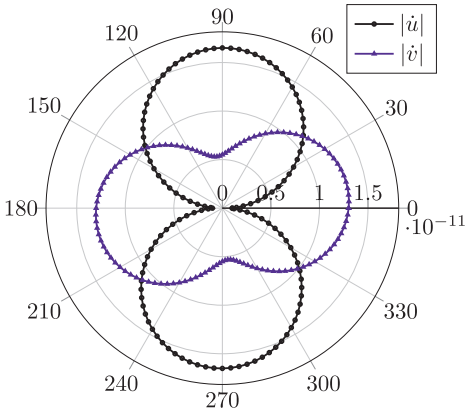

Fig. 9. Variations of the amplitudes of the S0 and A0 modes ($|\dot{u}|$ and $|\dot{v}|$) with the angle of the bias field (θ) at the left point, for the single-wire EMAT.

The polar plot corresponding to the left point in the middle plane of the plate is shown in Fig. 9. This plot seems like a mirror image of the previous plot so a detailed analysis is not necessary. From now on, only the plots at the right point will be shown.

4.2. The two-wire EMAT and the meander line EMAT

Next, we investigate the behavior of the two-wire EMAT in Fig. 1b. The idea is that with these two wires, an exact match between the wire distance and the one-half wavelength of the S0 mode could be achieved, which means the S0 mode waves will be added constructively if the currents are in opposite directions. Horizontally the two-wire structure is placed at the center of the model, and the phasors of the displacement components at the same right point are computed.

In Fig. 10, $|\dot{u}|$ and $|\dot{v}|$ curves are drawn for the two-wire EMAT when the distance of the wires is exactly half of the wavelength of the S0 mode and the currents are in opposite directions. The basic shapes of the curves are the same as in the previous case. The magnitude of $|\dot{u}|$ curve is around twice that of the curve for the single-wire EMAT. This is normal because now two wires with total currents of 1 A are working together (constructively) to generate the S0 mode waves.

The case of the two wires with currents in the same direction is also studied. The curves are shown in Figs. 11 and 12. These curves are drawn separately because their amplitudes have big difference and we don't want to simply draw the normalized curves. From Fig. 11 it could be observed that the S0 mode is now greatly weakened, while relatively the A0 mode is strengthened.

These results clearly show that match between the wire distance and

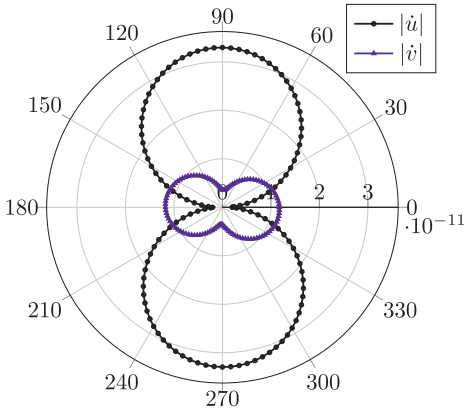

Fig. 10. Variations of the amplitudes of the S0 and A0 modes ($|\dot{u}|$ and $|\dot{v}|$) with the angle of the bias field (θ) at the right point, for the two-wire case, opposite currents.

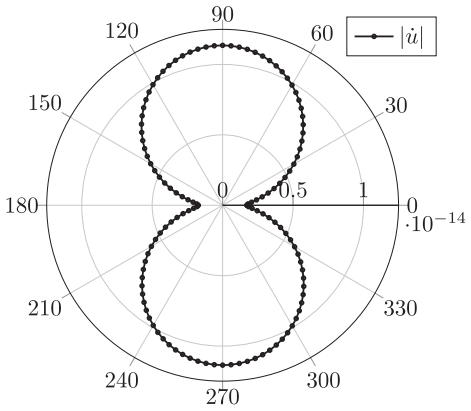

Fig. 11. Variation of the amplitude of the S0 mode ($|\dot{u}|$) with the angle of the bias field (θ) at the right point, for the two-wire case, currents in the same direction.

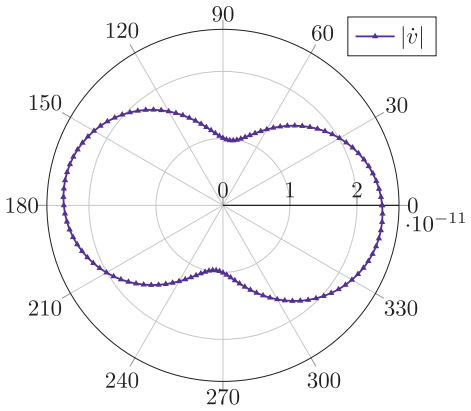

Fig. 12. Variation of the amplitude of the A0 mode ($|\dot{v}|$) with the angle of the bias field (θ) at the right point, for the two-wire case, currents in the same direction.

the one-half wavelength of the desired mode with opposite currents in the wires is helpful for generation of this mode while the same match with currents in the same direction will inhibit generation of this mode.

Then we can study the meander line EMAT (Fig. 4a). The coil is composed of 7 wires and the currents in two adjacent wires are in opposite directions. Now an assumption of uniform distribution of the bias field is no longer proper because we are not studying a 'building block' of a complex EMAT. The bias magnetic field is analyzed with a magnetostatic simulation. This also means that a polar plot of $|\dot{u}|$ and $|\dot{v}|$ is no longer possible since the bias magnetic field is now spatially distributed.

From Figs. 8 and 10, $|\dot{u}|$ and thus the S0 mode is excited mainly by the vertical bias field, or y component of the bias field. Distributions of the y component of the bias field B_{0y} at one-half skin depth in the plate for four different values of W_M are shown in Fig. 13. The range of x is $x \in [-W_C, W_C]$ with $W_C = 0.0667$ m. W_M takes the value of $0.5W_C$, W_C, $1.5W_C$ and $2W_C$ respectively. The positions of the wires represented by the small filled squares are also drawn. It could be observed how different the bias field could be with different values of W_M.

Then the width of the magnet is swept to check its influence on the generation of the Lamb wave modes. The $|\dot{u}|$ and $|\dot{v}|$ curves are shown in Fig. 14. The sweeping range is $W_M \in [0.5W_C, 2W_C]$. In fact, the $|\dot{u}|$ curve in Fig. 7 is part of the $|\dot{u}|$ curve in Fig. 14. It could be observed that the $|\dot{u}|$ curve reaches the maximum at W_M value a little bigger than W_C. The specific values are $W_M = 0.0783$ m and $W_C = 0.0667$ m, so the ratio $W_M/W_C = 117.39\%$. This result is similar to [9].

The maximum of the $|\dot{u}|$ curve in Fig. 14 could be explained by considering Figs. 10 and 13. With W_M increasing from $0.5W_C$, more and

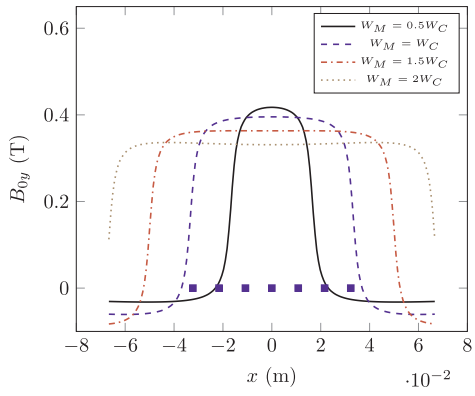

Fig. 13. Distributions of B_{0y}, for the meander line EMAT.

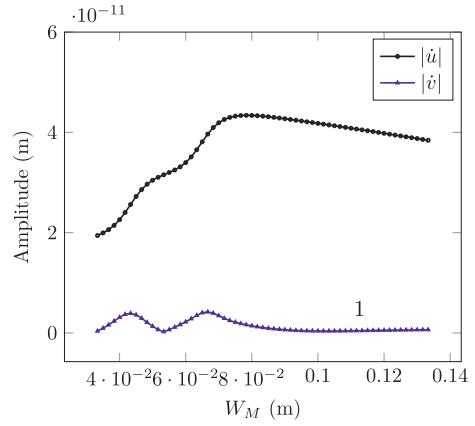

Fig. 14. Variations of $|\dot{u}|$ and $|\dot{v}|$ with W_M for the meander line EMAT.

more wires constructively generating the S0 mode waves are placed in the region of positive y component of the bias field, so the magnitude of $|\dot{u}|$ is increasing. When all the wires are placed in the region of the positive y component of the bias field, the magnitude of $|\dot{u}|$ begins to decrease because the magnitude of the positive y component of the bias field is dropping. This decrease after the initial increase leads to the maximum.

4.3. The wire bundle EMAT and the tightly wound EMAT

Besides the two-wire and the meander line structures where an exact match between the distance of adjacent wires and one-half wavelength of the desired Lamb wave mode is applied, there are also applications of EMATs in which the wires are tightly wound into a bundle. For these EMATs the spatial periodicity doesn't exist. Here we explore the idealized wire-bundle EMAT and the practical tightly wound EMAT. The only difference is that the bias field of the wire bundle EMAT is uniform, while the bias field of the tightly wound EMAT is distributed.

For the wire-bundle EMAT, if the width of the wire bundle (W_C) is exactly one-half wavelength of the S0 wave mode, then the situation is similar to the single-wire EMAT, and the difference is that now the multiple wires are placed closely and the eddy currents in the plate occupy a bigger region. The wire bundle of this EMAT is composed of 7 wires. The polar plots of the $|\dot{u}|$ and $|\dot{v}|$ curves corresponding to swept angle θ of the uniformly distributed bias magnetic field are shown in Figs. 15 and 16. They are drawn in different plots because they have very different amplitudes. The amplitude of $|\dot{u}|$ is several times that of the single-wire EMAT, because these wires work together constructively.

The case of a wire bundle with width of one wavelength of the S0 mode is also investigated. This is similar to the case of the two-wire EMAT with currents in the same direction. Now the number of the wires is 14. The polar plot of the $|\dot{u}|$ and $|\dot{v}|$ curves is shown in Fig. 17. As expected the S0 mode is severely weakened.

Finally a tightly wound EMAT containing a magnet and a coil of wire bundle with width of one-half wavelength of the S0 mode is modeled. The distributions of the y component of the bias field at one-half skin depth in the plate for four different values of W_M are shown in Fig. 18. The range of x is $x \in [-W_C, W_C]$ with $W_C = 0.01078$ m ($\frac{\lambda_{S0}}{2}$). W_M

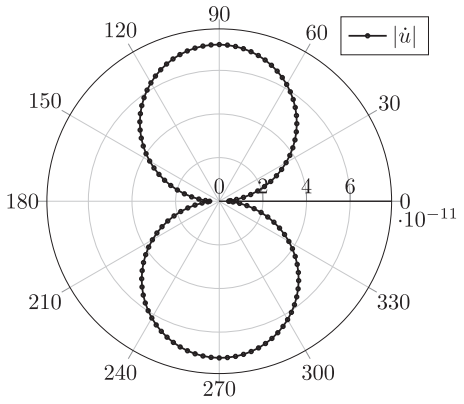

Fig. 15. Variation of the amplitude of the S0 mode ($|\dot{u}|$) with the angle of the bias field (θ) at the right point, for the wire bundle with width of one-half wavelength.

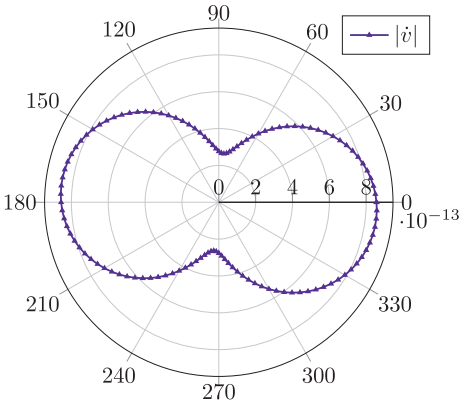

Fig. 16. Variation of the amplitude of the A0 mode ($|\dot{v}|$) with the angle of the bias field (θ) at the right point, for the wire bundle with width of one-half wavelength.

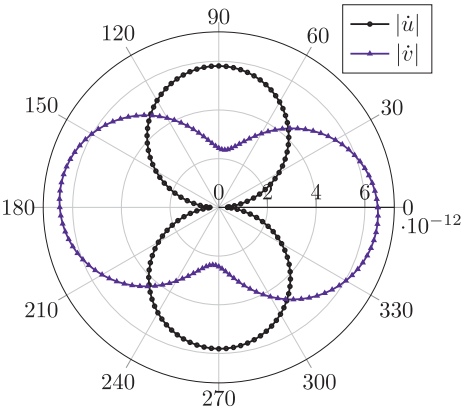

Fig. 17. Variations of the amplitudes of the S0 and A0 modes ($|\dot{u}|$ and $|\dot{v}|$) with the angle of the bias field (θ) at the right point, for the wire bundle with width of one wavelength.

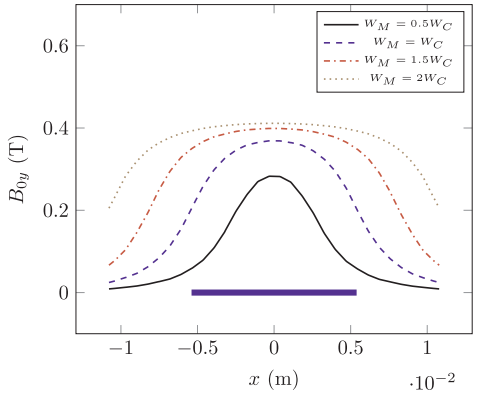

Fig. 18. Distributions of B_{0y}, for the tightly wound EMAT.

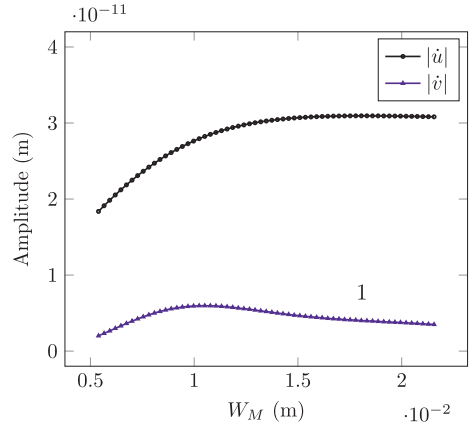

Fig. 19. Variations of $|\dot{u}|$ and $|\dot{v}|$ with W_M for the tightly wound EMAT with coil width of one-half wavelength.

takes the value of $0.5W_C$, W_C, $1.5W_C$ and $2W_C$ respectively. The range of the wire bundle is represented by the horizontal line section on the x axis.

Then the width of the magnet is swept. The $|\dot{u}|$ and $|\dot{v}|$ curves are shown in Fig. 19. The sweeping range is $W_M \in [0.5W_C, 2W_C]$.

The behavior of the $|\dot{u}|$ curve in Fig. 19 could be explained by considering Figs. 15 and 18. With W_M increasing from $0.5W_C$, the magnitude of the y component of the bias field at the wires is increasing, so the magnitude of $|\dot{u}|$ is also increasing. When all the wires experience almost equal magnitude of B_{0y}, further increase in W_M leads to minor increase in the magnitude of B_{0y}, so the magnitude of $|\dot{u}|$ tends to enter the zone of 'saturation'.

It should be noted that all the results are for specific combinations of the parameters including the frequency, the thickness of the plate, the electromagnetic and elastic properties of the materials in the models, etc. Nevertheless, some results are universal. More importantly, this work presents methodology to solve the proposed fundamental problem in the study and application of the EMATs.

In this work we focus on the frequency domain model with which the excitability of Lamb waves could be characterized easily. Readers interested in the interaction of the generated waves with simulated defect could refer to [12] where the focus was mainly on the time domain model, which is suitable for this problem. In that work a crack-like slot defect with a rectangular cross section was considered. The input S0 mode wave was generated by a meander coil EMAT, and transmitted and reflected S0 and A0 mode Lamb waves could be observed.

5. Conclusion

EMATs are versatile non-contact ultrasonic transducers capable of generating various wave modes and could be used to test hot and moving samples, but their transduction efficiency is low. Truly coupled models of the EMATs are valuable for research and applications but modeling of the EMATs is not easy because electromagnetic and elastodynamic effects are coupled together.

One fundamental and important problem in the study and application of EMATs for plate inspection using Lamb waves is how the configuration of the EMAT influences the generation of different Lamb wave modes. A model-based solution to this problem requires that the model should be truly coupled so that it is correct and accurate theoretically, and it should also be convenient to evaluate the model. Besides these, a method should be devised to separate the S0 and A0 modes of Lamb waves effectively.

In this work, we built coupled models for idealized and practical EMATs. By 'ideal' we mean the bias magnetic field is uniformly distributed and the direction of the bias field could be swept. By 'practical' we mean the magnet is modeled explicitly so the bias field is distributed. The amplitudes of the Lamb wave modes are chosen for characterizing the excitability of Lamb waves. For this end we compared three methods to calculate the displacement components u and v corresponding to the S0 mode and the A0 mode respectively, at a point in the middle plane of the plate. The time-domain simulation is straightforward but very time-consuming. The multi-frequency method is less time-consuming but still involves multiple frequency components. The single frequency method is the fastest and is used extensively for characterizing the EMATs.

With the single frequency approach, the idealized EMATs including the single-wire EMAT, the two-wire EMAT and the wire bundle EMAT (all with uniform bias field), and the practical EMATs including the meander line EMAT and the tightly wound EMAT (both with distributed bias field) are studied. For the idealized EMATs, polar plots of the $|\dot{u}|$ and $|\dot{v}|$ curves with respect to the angle θ of the bias field are generated. For all the idealized EMATs, the $|\dot{u}|$ curves have similar shapes. The $|\dot{v}|$ curves are also similar. $|\dot{u}|$ increases from around zero with θ increasing from 0° to 90°, and then decreases to around zero with θ increasing from 90° to 180°. The other part of the curve is symmetric with respect to the line representing $\theta = 0^\circ$ and $\theta = 180^\circ$. The $|\dot{v}|$ curve has similar shape, the difference is that it is rotated 90° and the minimum value of $|\dot{v}|$ is not near zero. These results indicate that horizontal bias field generates almost no S0 mode waves and maximum A0 mode waves, while vertical bias field generates maximum S0 mode waves and some A0 mode waves, so the S0 mode waves are mainly decided by the y component of the bias field. These results also show that match between the distance of the two wires in the two-wire EMAT and the one-half wavelength of the S0 mode with currents of the wires in opposite directions strengthens the S0 mode generation, while if the currents are in the same direction, the S0 mode is weakened. Similarly, if the width of the wire bundle in the wire-bundle EMAT is one-half wavelength, the S0 mode is strengthened, while if the width of the wire bundle is exactly one wavelength, the S0 mode is weakened.

For the practical EMATs, the width of the magnet is swept. For the meander line EMAT, there is a maximum in the $|\dot{u}|$ curve at magnet width of 117.39% of the coil width. For the tightly wound EMAT, the $|\dot{u}|$ curve saturates with increasing magnet width. These phenomena could be explained from the distribution of the y component of the bias magnetic field, at a horizontal line at one-half skin depth of the plate.

Besides presenting results for the specific parameters of the models, this work provides methodology to solve the proposed problem of characterizing excitability of Lamb waves generated by the EMATs with a model-based approach.

Acknowledgment

This work was financially supported by the National Key Scientific Instrument and Equipment Development Project (Grant No. 2018YFF01012802) and the National Natural Science Foundation of China (Grant Nos. 51777100 and 51677093).

References

[1] R. Thompson, Model for electromagnetic generation and detection of Rayleigh and Lamb waves, IEEE Trans. Sonics Ultrason. SU20 (4) (1973) 340–346.
[2] R. Thompson, Mechanisms of electromagnetic generation and detection of ultrasonic Lamb waves in iron-nickel alloy polycrystals, J. Appl. Phys. 48 (12) (1977) 4942–4950.
[3] H. Ogi, M. Hirao, T. Ohtani, Line-focusing of ultrasonic SV wave by electromagnetic acoustic transducer, J. Acoust. Soc. Am. 103 (5, 1) (1998) 2411–2415.
[4] K. Mirkhani, C. Chaggares, C. Masterson, M. Jastrzebski, T. Dusatko, A. Sinclair, R. Shapoorabadi, A. Konrad, M. Papini, Optimal design of EMAT transmitters, NDT & E Int. 37 (3) (2004) 181–193.
[5] ASTM. E 1774 96 Standard Guide for Electromagnetic Acoustic Transducers (EMATs) - An American National Standard, Standard. American Society for Testing and Materials; 1997.
[6] A. Sophian, R. Edwards, G. Tian, S. Dixon, Dual-probe methods using pulsed eddy currents and electromagnetic acoustic transducers for NDT inspection, Insight 47 (6) (2005) 341–345.
[7] R. Edwards, A. Sophian, S. Dixon, G. Tian, X. Jian, Dual EMAT and PEC non-contact probe: applications to defect testing, NDT & E Int. 39 (1) (2006) 45–52.
[8] R. Ludwig, X. Dai, Numerical-simulation of electromagnetic acoustic transducer in the time domain, J. Appl. Phys. 69 (1) (1991) 89–98.
[9] M. Kaltenbacher, R. Lerch, H. Landes, K. Ettinger, B. Tittmann, Computer optimization of electromagnetic acoustic transducers, in: S. Schneider, M. Levy, B. McAvoy (Eds.), 1998 IEEE Ultrasonics Symposium - Proceedings, Ultrasonics Symposium, IEEE; Ultrason Ferroelect & Frequency Control Soc, vols. 1 and 2, 1998, pp. 1029–1034 (1998 IEEE Ultrasonics Symposium, SENDAI, JAPAN, OCT 05–08, 1998).
[10] M. Kaltenbacher, K. Ettinger, R. Lerch, B. Tittmann, Finite element analysis of coupled electromagnetic acoustic systems, IEEE Trans. Magn. 35 (3, 1) (1999) 1610–1613 8th Biennial IEEE Conference on Electromagnetic Field Computation (IEEE CEFC 98), Tucson, Arizona, Jun 01–03, 1998..
[11] R. Jafari-Shapoorabadi, A. Konrad, A. Sinclair, Improved finite element method for EMAT analysis and design, IEEE Trans. Magn. 37 (4, 1) (2001) 2821–2823 8th Joint Magnetism and Magnetic Materials International Magnetics Conference (MMM-INTERMAG), San Antonio, Texas, Jan 07–11, 2001..
[12] S. Wang, S. Huang, Y. Zhang, W. Zhao, Multiphysics modeling of a lorentz force-based meander coil electromagnetic acoustic transducer via steady-state and transient analyses, IEEE Sens. J. 16 (17) (2016) 6641–6651.
[13] R. Dhayalan, K. Balasubramaniam, A hybrid finite element model for simulation of electromagnetic acoustic transducer (EMAT) based plate waves, NDT & E Int. 43 (6) (2010) 519–526.
[14] P.B. Nagy, F. Simonetti, G. Instanes, Corrosion and erosion monitoring in plates and pipes using constant group velocity Lamb wave inspection, Ultrasonics 54 (7) (2014) 1832–1841.
[15] M. Seher, P. Huthwaite, M. Lowe, P. Nagy, P. Cawley, Numerical design optimization of an EMAT for A0 Lamb wave generation in steel plates, in: D. Chimenti, L. Bond, D. Thompson (Eds.), 40th Annual Review of Progress in Quantitative Nondestructive Evaluation: Incorporating the 10th International Conference on Barkhausen Noise and Micromagnetic Testing, vols. 33A & 33B, vol. 1581 of AIP Conference Proceedings, 2014, pp. 340–347.
[16] M. Seher, P. Huthwaite, M.J.S. Lowe, P.B. Nagy, Model-based design of low frequency Lamb wave EMATs for mode selectivity, J. Nondestruct. Eval. 34 (3) (2015).
[17] N. Ida, Engineering Electromagnetics, Springer, 2007.
[18] R. Jafari-Shapoorabadi, A. Sinclair, A. Konrad, Finite element determination of the absolute magnitude of an ultrasonic pulse produced by an EMAT, in: S. Schneider, M. Levy, B. McAvoy (Eds.), 2000 IEEE Ultrasonics Symposium Proceedings, Ultrasonics Symposium, IEEE Ultrason, Ferroelect, & Frequency Control Soc, Vols 1 and 2, 2000, pp. 737–741 (IEEE Ultrasonics Symposium, San Juan, PR, Oct 22–25, 2000).
[19] A. Konrad, The numerical-solution of steady-state skin effect problems - an integrodifferential approach, IEEE Trans. Magn. 17 (1) (1981) 1148–1152.
[20] B.A. Auld, Acoustic Fields and Waves in Solids, Krieger Publishing Company, 1990.
[21] L.W. Schmerr, Fundamentals of Ultrasonic Nondestructive Evaluation: A Modeling Approach, Springer, 1998.
[22] P. Wilcox, M. Lowe, P. Cawley, The excitation and detection of lamb waves with planar coil electromagnetic acoustic transducers, IEEE Trans. Ultrason. Ferroelectr. Freq. Control 52 (12) (2005) 2370–2383.
[23] S. Wang, S. Huang, A. Velichko, P. Wilcox, W. Zhao, A multi-objective structural optimization of an omnidirectional electromagnetic acoustic transducer, Ultrasonics 81 (2017) 23–31.